ADVANCED SUSTAINABLE SYSTEMS
www.advsustainsys.com

Probing Enhanced Electrochemical Performance of Poly (3,4-ethylenedioxy Thiophene) Encapsulated 5.3 V Spinel $LiCoMnO_4$ Cathode for Li-ion Batteries

Sreekumar Sreedeep, Yun-Sung Lee, and Vanchiappan Aravindan**

Herein, the effect of poly(3,4-ethylenedioxythiophene) polystyrene sulfonate (PEDOT) coating is reported on the electrochemical properties of high voltage, 5.3 V lithium cobalt manganese oxide ($LiCoMnO_4$, LCMO) cathodes. Scalable precipitation followed by a wet coating method is employed for the synthesis of LCMO@PEDOT. Various analytical studies are performed to validate the performance of the cathode. The cycling profile exhibits an enhanced electrochemical performance among the LCMO@PEDOT compared to that of pristine LCMO in a half-cell configuration. Also, the LCMO@PEDOT: 0.5–3 wt.% is optimized to show better electrochemical performance. The diffusion coefficient calculated from both cyclic voltammetry and electrochemical impedance spectroscopy (EIS) exhibits an increase in the magnitude from PEDOT coating of 0.5 to 3 wt.% in the order of $\approx 10^{-12}$ cm^2 s^{-1}. An in-operando X-ray diffraction and in-situ EIS are performed to validate the electrochemical activity. The full-cell assembly is also fabricated with spinel $Li_4Ti_5O_{12}$ (LTO) anode under balanced loading conditions. The LCMO@PEDOT (1–3 wt.%)/LTO exhibits better electrochemical performance compared to pristine LCMO/LTO. In addition, a temperature study of full-cell is carried out within the range of −10 to 20 °C and compared.

1. Introduction

The 20th century has been marked by the development of portable electronics, emission-free electric vehicles, and numerous renewable energy technologies.[1–4] The advancement in Lithium-ion batteries (LIBs) played a vital role in powering up modern-day development, resulting in a growing demand to increase the power and energy density of LIBs. Conventional cathodes such as $LiCoO_2$ have been associated with setbacks like the high cost of Co, limited Li-extraction, and poor safety limits, which have motivated the search for alternate cathode materials. Even though progressive advancements in olivine-structured $LiMPO_4$ (M: Mn, Fe, and Co) have led to the commercialization of $LiFePO_4$ by considering the utmost cell safety, the low redox potential (3.4 V vs Li) of the $Fe^{3+/2+}$ couple has resulted in poor (theoretical) energy density.[5–11] Recently, the spinel-structured $LiCoMnO_4$, owing to the high theoretical capacity of 145 mAh g^{-1} and high operating voltage of 5.3 V vs Li, has attracted attention as a promising cathode for LIB.[12–15] In addition, the low volume change of 0.7% occurring during charge–discharge makes it more electrochemically stable.[13] Although found attractive as a promising cathode, the commercialization of $LiCoMnO_4$ is still not achieved owing to the poor coloumbic efficiency, fast capacity decay, and co-existence of insulating Li_2MnO_3 components. Hence, to mitigate these undesirable electrochemical properties, several strategies have to be implemented, of which the method of surface coating is found to be more promising.

Considering the nature of coating materials, they can be classified into several categories, such as oxides, fluorides, phosphates, carbon, and polymer-based materials. Also, the coating imparts several desirable properties, including enhancing electrochemical stability, preventing the parasitic side-reaction between cathode and electrolyte, and suppressing metal dissolution. Lai et al.[16] observed an enhancement in the electrochemical performance of $LiNi_{0.8}Co_{0.15}Al_{0.05}O_2$ (NCA) upon polymer-coating with Poly (3-hexylthiophene-2,5-diyl) (P3HT) with a capacity retention of 90 and 80% after 100 and 1000 cycles, respectively. Also, Wang et al.[17,18] observed an enhancement in the cycle stability in $Li[Li_{0.2}Fe_{0.1}Ni_{0.15}Mn_{0.55}]O_2$ on coating with $AlPO_4$. Hence, showing the importance of surface coating improves the electrochemical properties of the high-voltage cathodes.

The use of conducting polymers such as Polyaniline (PANI),[19] Polypyrolle,[20] and Poly (3,4 – ethylene dioxythiophene) (PEDOT)[21] plays a positive role in enhancing the electrochemical performance of the material. The PEDOT: PSS with

S. Sreedeep, V. Aravindan
Department of Chemistry
Indian Institute of Science Education and Research (IISER)
Tirupati 517507, India
E-mail: aravindan@iisertirupati.ac.in
Y.-S. Lee
School of Chemical Engineering
Chonnam National University
Gwang-ju 61186, Republic of Korea
E-mail: leeys@chonnam.ac.kr

The ORCID identification number(s) for the author(s) of this article can be found under https://doi.org/10.1002/adsu.202300267

DOI: 10.1002/adsu.202300267

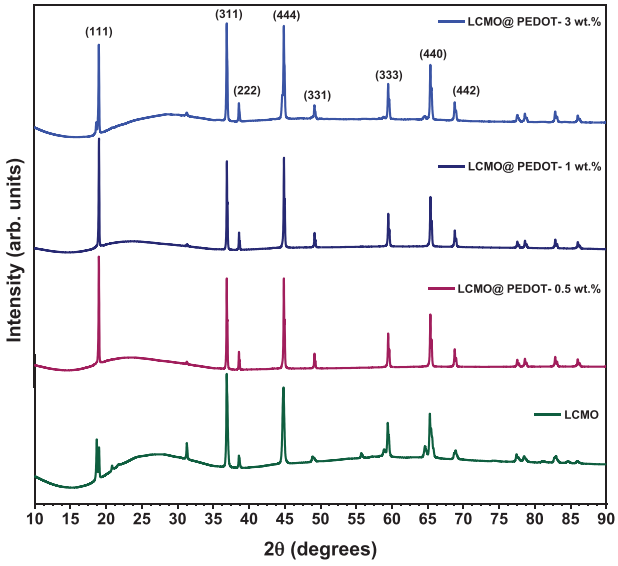

Figure 1. XRD pattern of pristine LCMO and composites LCMO@PEDOT: 0.5–3 wt.%.

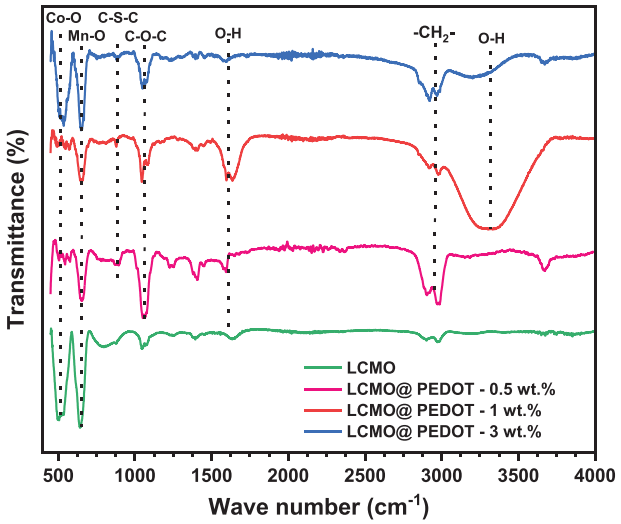

Figure 2. FT-IR spectra of LCMO and the composites LCMO@PEDOT: 0.5–3 wt.%.

PEDOT carrying a positive charge and PSS carrying a negative charge enhances the electrochemical stability as well as conductivity of the material. Wu et al.[22] have reported that the surface coating of PEDOT: PSS on $Li[Li_{0.2}Ni_{0.2}Mn_{0.6}]O_2$ has enhanced the capacity retention to about 51.6% after 100 cycles. Also, the use of PEDOT: PSS has also improved sulfur utilization and capacity retention in a Li–S battery.[23] Apart from its use as a conductive polymer, the PEDOT: PSS also shows the functionality of a binder; hence, it can be used as a dual-functional polymer for LIBs, which can enhance the conductivity and improve the adhesion of the electrode with the current collector.

Hence, taking into account the various setbacks associated with $LiCoMnO_4$, an attempt has been made to overcome these challenges by using an ex-situ PEDOT: PSS polymer coating. The $LiCoMnO_4$ has been synthesized by a scalable precipitation method followed by an ex-situ coating of PEDOT: PSS. In addition, the in-operando XRD has been done to study the structure and phase change happening during the charge–discharge process.[24] Also, comparing the diffusion coefficient calculated from Cyclic Voltammetry (CV) and Electrochemical Impedance Spectroscopy (EIS) has proved the efficiency of PEDOT: PSS coating. Additionally, the full-cell fabrication has been carried out with $Li_4Ti_5O_{12}$ (LTO) as an anode, and the temperature study of the same has been carried out within the range of −10 to 20 °C.

2. Results and Discussion

The powder XRD analysis (**Figure 1**) has been carried out to determine the structural features of the as-synthesized pristine LCMO and LCMO@PEDOT: 1–3 wt.%. The XRD peaks of the composite LCMO@PEDOT: 1–3 wt.% is consistent with that of pristine LCMO, revealing that the crystal structure of LCMO has been maintained even after surface modification with PEDOT. Adding to this, the prominent diffraction peaks at 2θ values of 19.2°, 37°, 45.8°, and 65.5° correspond to the (111), (311), (444), and (440) crystal planes, which indicates the formation of cubic spinel structure with an Fd3m space group.[12] Further, the Fourier transform infrared (FT-IR) spectra have been analyzed for both LCMO and LCMO@PEDOT: 0.5–3 wt.%, as shown in **Figure 2**. Due to the relatively low content of PEDOT coating, there was no substantial change in the IR spectra of the composites compared to that of pristine LCMO. The strong and broad peak at ≈3300 cm^{-1} is attributed to the stretching vibrations, and the less intense peak observed at ≈1632 cm^{-1} is due to the bending vibrations of the O—H bond of H_2O present in the solution.[16,21,22,25] In addition, the absorption bands observed at ≈890, ≈1061, and ≈2960 cm^{-1} mark the presence of C—S—C, C—O—C, and —CH_2— which are characteristic peaks of PEDOT, hence showing the formation of a PEDOT coating on LCMO. The more intense peaks observed at ≈520 and ≈650 cm^{-1} are attributed to Co—O and Mn—O stretching bands of both LCMO and LCMO@PEDOT. The Raman spectra (Figure S1, Supporting Information) of LCMO@PEDOT exhibit a strong band close to ≈622 cm^{-1} and a group of relatively weak bands in the 200–500 cm^{-1} region. In the oxide and Manganese oxide-based spinels, the bands observed at ≈600–650 cm^{-1} are attributed to the vibrational motion of oxygen atoms in the MnO_6 octahedra.[8–10,26] Hence, the high-intensity band observed at ≈625 cm^{-1} is marked by the presence of Mn—O stretching vibration in MnO_6 octahedra, and this vibration is assigned as A_{1g} vibration mode in $O_h{}^7$ spectroscopic group. In addition, the less intense peaks at ≈479 and 521 cm^{-1} are attributed to the $3F_{2g}$, E_g mode of the Co—O stretching vibration. The determination of the surface elemental composition of LCMO@PEDOT was further carried out by XPS analysis. The XPS survey spectrum (**Figure 3**a–f) marks the presence of elements such as Li, Co, Mn, O, and C. The deconvolution of the core level of Li 1s, Co 2p, Mn 2p, O 1s, and C 1s gives the chemical state of the elements. The deconvolution of C 1s core level indicates peaks at 284.6, 286, and 289.3 eV, corresponding to C═C, C—C, and O—C═O, respectively. Also, the decomposition O 1s core level yield peaks positioned at 529.8, 531.6, and 534.4 eV, corresponding to M—O (Co—O, Mn—O), C—O, and C═O, respectively. Adding to this, the deconvolution of transition metal core levels of Mn 2p and Co 2p

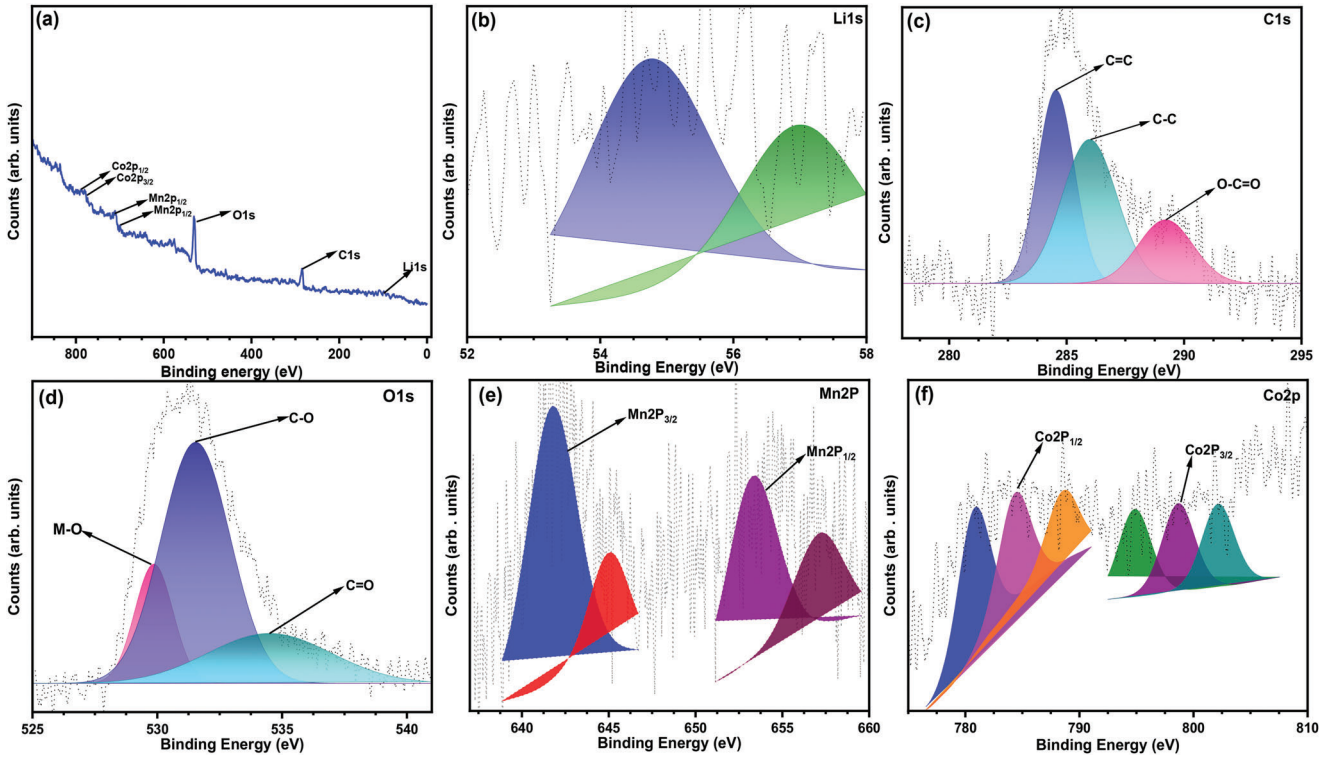

Figure 3. a) High-resolution XPS spectra of the as-synthesized LCMO@PEDOT composites showing the elements present b–f) XPS spectra of Li 1s, C 1s, O 1s, Mn 2p, and Co 2p.

yields peaks corresponding to Mn $2p_{3/2}$, Mn $2p_{1/2}$ and Co $2p_{3/2}$, Co $2p_{1/2}$, which indicates an oxidation state of +4 and +3 respectively.

The FE-SEM and TEM (**Figure 4**a–f) imaging studies have been performed to analyze the morphological as well as structural aspects of LCMO@PEDOT. The FE-SEM shows a non-uniform distribution of spherical-shaped LCMO@PEDOT particles with a particle size of 1.6 µm. Also, the FE-SEM images depict a uniform PEDOT polymer coating on the surface of the sample, which is further revealed by the TEM analysis. In addition, the interlayer spacing has been calculated from the TEM image as 2.48 Å, corresponding to the (311) crystal plane of the LCMO lattice. The crystalline nature of the sample has been further confirmed by the selected area electron diffraction pattern (SAED). The energy dispersion X-ray spectroscopy (EDS) (Figure 4g–k) indicates a homogenous distribution of Mn, Co, O, S, and C elements throughout the sample.

2.1. Half-Cell Performance

The half-cell performance for both pristine LCMO and the composite LCMO@PEDOT: 0.5–3 wt.% has been carried out within a potential window of 3.5–5.2 V vs Li at a current density of 20 mA g^{-1}. The cycling profile data shows an enhancement in the electrochemical performance among the PEDOT-coated composites compared to pristine LCMO, which is attributed to the formation of a uniform polymer framework on the surface of cathode particles, thereby preventing the unfavorable parasitic side-reactions with the electrolyte, hence improving the cycle stability and rate capability. The mechanism underlying the enhancement of electrochemical performance upon the PEDOT coating can be accounted for by the trapping of F^- anions formed by the auto decomposition of $LiPF_6$ by the Sulfur atom present in the polymer, thereby mitigating the transition metal dissolution in the form of electrolyte soluble compounds due to nucleophilic attack of F^- anions. The Galvanostatic charge–discharge (GCD) (**Figure 5**a,b) further reveals a poor capacity retention of 45% for the pristine LCMO after 80 cycles, though it exhibits a good discharge capacity of 105 mAh g^{-1}, whereas the 0.5, 1, and 3 wt.% PEDOT modification exhibits better capacity retentions of 70, 72, and 75% after 80 cycles with discharge capacities of 113, 114, and 109 mAh g^{-1}, respectively. Adding to this, the rate performance study (Figure 5c,d) further illustrates an enhancement in the rate capability and cycle stability even at a high current density of 70 and 100 mA g^{-1} with excellent capacity retention among the LCMO@PEDOT: 0.5–3 wt.% compared to pristine LCMO. Although found attractive as a promising conductive polymer, screening the optimal concentration of PEDOT is more important as the thin PEDOT coating is less effective toward preventing the parasitic side-reactions, whereas a thick coating layer enhances the Li^+ ion conduction and also prevents the LCMO from parasitic side-reactions. Hence, based on the cyclability results, the 1 and 3 wt.% of PEDOT can be optimized to be the better coating composition on the surface of LCMO.

The cyclic voltammetry (CV) (Figure S2, Supporting Information) study has been conducted for both the pristine LCMO and the LCMO@PEDOT: 0.5–3 wt.% composite at a scan rate of

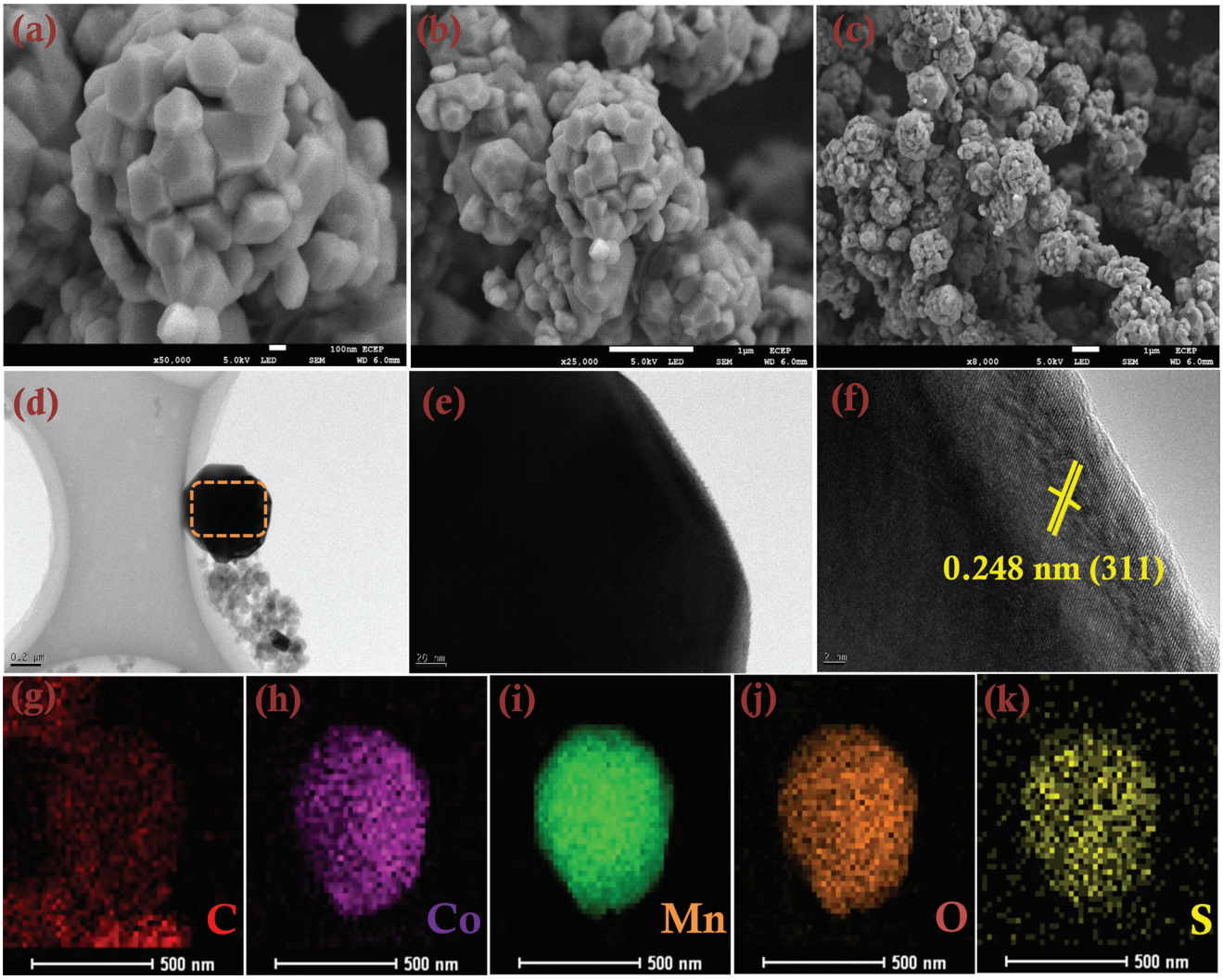

Figure 4. a–c) FE-SEM images of LCMO@PEDOT, d–f) HR-TEM images of LCMO@PEDOT, and g–k) EDS elemental mapping of LCMO@PEDOT, showing the elemental distribution of C, Co, Mn, O, and S.

0.1 mV s^{-1}. The CV exhibits two pairs of oxidation peaks at 4 and 5.1 V vs Li along with two pairs of reduction peaks at 3.8 and 4.7 V vs Li corresponding to Mn^{3+}/Mn^{4+} and Co^{3+}/Co^{4+} redox couple, which is consistent with the GCD profile of LCMO. In addition, it can be further observed from the CV that the Co^{3+}/Co^{4+} oxidation peaks undergo a slight shift toward lower potential as the amount of PEDOT is increased from 0.5 to 3 wt.%, whereas a pronounced peak shift can be observed in the case of pristine LCMO. Hence, this observation accounts for the reduction in polarization upon PEDOT coating compared to the pristine LCMO, while the extent of polarization decreases as the amount of PEDOT coating increases from 0.5 to 3 wt.%.

The Electrochemical impedance spectroscopy (EIS) study has been performed to determine the kinetics of electrochemical reactions of LCMO@PEDOT composite. The Nyquist plots for the different concentrations of PEDOT from 0.5–3 wt.%, along with their respective equivalent circuit at different temperatures of −10 to 25 °C have been illustrated in (**Figure 6**a–d). The Nyquist plots at moderate temperatures of 10 and 25 °C exhibit an equivalent-circuit consisting of an uncompensated ohmic resistance or solution resistance (R_Ω), resistance due to cathode electrolyte interphase (R_{CEI}), charge-transfer resistance (R_{CT}), and a constant phase element (Q) at the high-frequency region along with a rising Warburg (Z_W) at the low-frequency region. But at low temperatures of 0 and −10 °C, the Nyquist plot consists of an R_Ω, R_{CEI}, R_{CT}, and Q in the high-frequency region, whereas the low-frequency Warburg (Z_W) region is absent owing to the sluggish diffusion of Li^+–ions at low temperatures. However, irrespective of the temperature, the Nyquist plots exhibit a similar trend with a higher value of R_{CT} for pristine LCMO compared to that of LCMO@PEDOT composites, while an increase in the R_{CT} value can be observed as the amount of PEDOT coating increases from 0.5 to 3 wt.%. The comparison of the Nyquist plots further exhibits a higher value of R_{CT} at low temperatures owing to the freezing-up of electrolytes, which hinders the Li^+ ion diffusion process. However, at moderate and high temperatures, the thermal energy enhances the Li^+ ion diffusion, thereby lowering the R_{CT} value. To further investigate the effect of PEDOT coating on

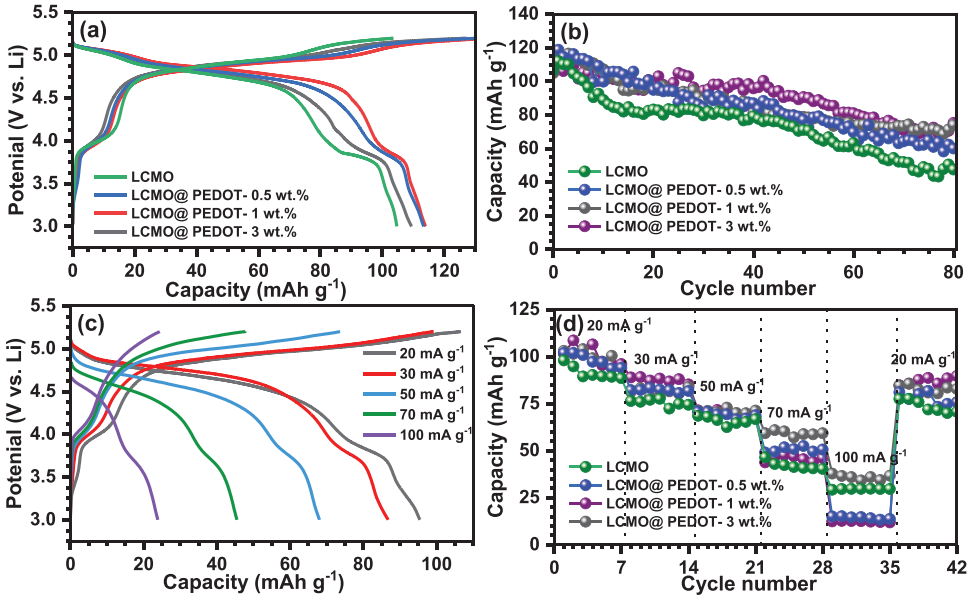

Figure 5. Half-cell performance: a) Galvanostatic charge–discharge curve at a current density of 20 mA g^{-1}, b) Capacity vs cycle number plots of LCMO and LCMO@PEDOT: 0.5–3 wt.% at a current density of 20 mA g^{-1}, c) charge–discharge curves of LCMO@PEDOT- 3 wt.% at current densities of 20, 30, 50, 70, and 100 mA g^{-1} and d) Rate-performance study of pristine LCMO and LCMO@PEDOT: 0.5–3 wt.%.

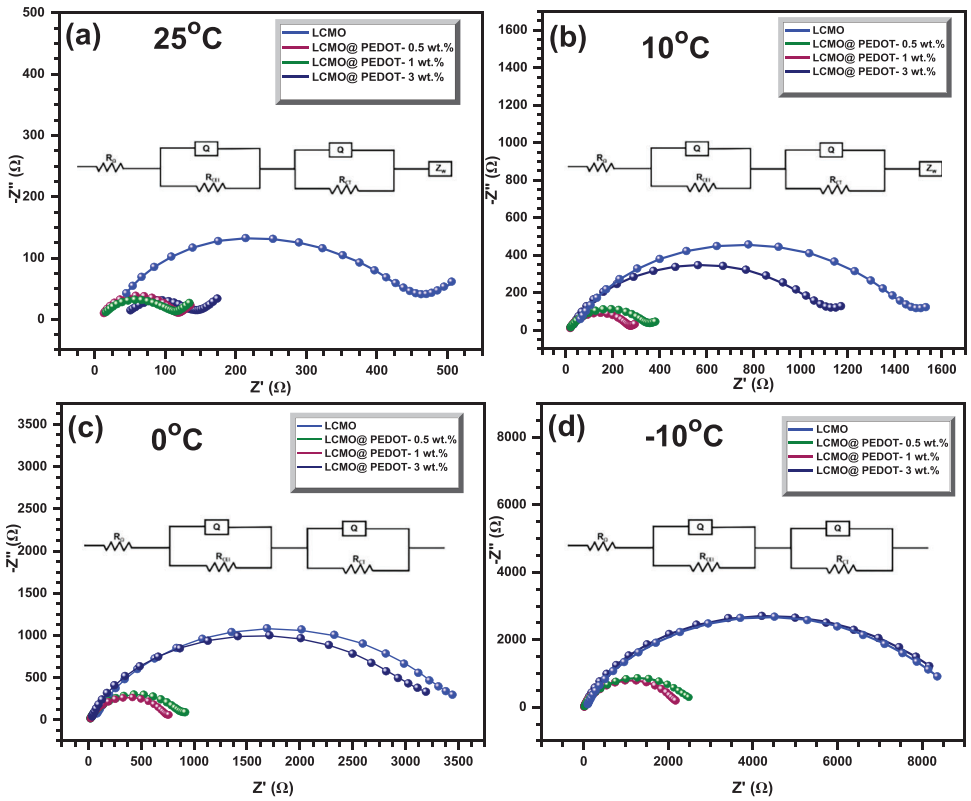

Figure 6. a–d) Nyquist plots of LCMO and composites LCMO@PEDOT: 0.5–3 wt.% at different temperatures ranging from −10 to 25 °C along with their corresponding equivalent circuits at a frequency ranging from 0.1 Hz to 10 kHz.

the electrochemical performance of LCMO, an in-situ impedance (Figure S3a–j, Supporting Information) has been conducted in a half-cell assembly. The in-situ impedance study has been done to analyze the nature of the polymer coating and the cathode-electrolyte interphase (CEI) as the cycling progresses. From the in-situ impedance profile, it is evident that there is a slight increase in the R_{CT} during the initial 1st to the 10th cycle due to the combined resistance of the formed CEI layer and the PEDOT coating. However, as the cycling progresses from the 10th to 50th and then to the 100th cycle, the R_{CT} value remains almost constant, as the PEDOT coating effectively suppresses the parasitic reactions which lead to the formation of side-products such as Li_2CO_3 and LiF, hence providing a better channel for the Li^+ ion diffusion.

The apparent Li^+ ion diffusion coefficient has been determined from both EIS and CV plots. From the Nyquist plot, the low-frequency Warburg region indicates the resistance toward Li^+ ion diffusion, and the diffusion coefficient is calculated from the slope of the Z vs $\omega^{-1/2}$ (Figure S4, Supporting Information) using the equation-

$$D_{Li}^{+} = R^2T^2/2\ A^2n^4F^4\sigma_w^2C^2 \quad (1)$$

where R is the universal gas constant, T is the temperature, A is the cross-sectional area of the electrode, n is the number of Li^+ ions involved in charge–discharge, F is the Faraday constant (96,485 C mol^{-1}), σ_w is the slope of the curve or Warburg constant, C is the concentration of the electrolyte.[14,27–29] The values of $D_{Li}{}^+$ (Table S2, Supporting Information) show a magnitude in the order of $\approx 10^{-13}$ cm^2 s^{-1}. The as-determined value of $D_{Li}{}^+$ exhibits an increase in the trend from 2.17×10^{-13} to 3.77×10^{-13} cm^2 s^{-1} among the pristine LCMO to LCMO@PEDOT- 2 wt.% composites, while a slight decrease in the magnitude of $D_{Li}{}^+$ to 3.54×10^{-13} cm^2 s^{-1} can be observed for LCMO@PEDOT- 3 wt.% owing to the thicker PEDOT coating which resists the Li^+ ion diffusion.

To further validate the result obtained from EIS, the apparent Li^+ ion diffusion coefficient has been evaluated from the CV at scan rates ranging from 0.1 to 1 mV s^{-1}. From the CV, the diffusion coefficient is calculated from the slope of the I_p vs $v^{1/2}$ (Figure S5, Supporting Information) graph using the Randles-Sevciks equation -

$$I_p = 2.69 \times 10^5 n^{3/2} C_o A D^{1/2} v^{1/2} \quad (2)$$

where I_p is the peak current (cathodic or anodic), n is the number of Li^+ ions involved in charge–discharge, C_o is the electrolyte concentration, A is the electrode area, D is the diffusion coefficient, and v is the square root of scan rate. As expected, the diffusion coefficient exhibits an increase in the trend from pristine LCMO to LCMO@PEDOT- 1 wt.% (Table S1, Supporting Information) as 1.8×10^{-13} to 2.2×10^{-13} cm^2 s^{-1} along with a marginal decrease to 2.0×10^{-13} cm^2 s^{-1} for LCMO@PEDOT- 3 wt.%. Hence, the diffusion coefficient obtained from CV exhibits a similar trend as that obtained from the EIS.

The kinetics of the electrochemical reaction have been evaluated from the Arrhenius plot by comparing the activation energy for the pristine LCMO and the LCMO@PEDOT: 0.5–3 wt.%. From the ln(σ) vs 1000/T plot (Figure S6, Supporting Information), the activation energy has been calculated from its slope using the equation,

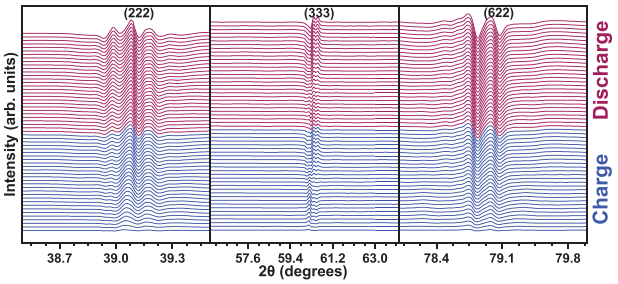

Figure 7. In-situ XRD analysis of LCMO@PEDOT.

$$\ln(\sigma) = \ln(\sigma_o) - E_a/1000RT \quad (3)$$

where σ is the conductance, σ_o is the pre-exponential factor, E_a is the activation energy (eV), R is the universal gas constant (R = 8.314 kJ mol^{-1}), and T is the temperature (in kelvin). The activation energy (Table S3, Supporting Information) exhibits a decrease in its magnitude from pristine LCMO to LCMO@PEDOT: 0.5–1 wt.% as 0.33, 0.25, and 0.15 eV, while a slight increase in its value to 0.22 eV can be observed in the case of LCMO@PEDOT-3 wt.%. Hence, the trend in activation energy further validates the diffusion coefficient obtained from both CV and EIS with an increase in the Li^+ ion kinetics from the pristine LCMO to LCMO@PEDOT- 1 wt.%, along with a slight decrease in the kinetics in the case of LCMO@PEDOT- 3 wt.%.

To understand the dynamic phase evolution and to validate the mechanism of Li-insertion/de-insertion accompanying the charge–discharge of LCMO@PEDOT, An in-operando powder XRD (**Figure 7**) has been carried out within a potential range of 3.5–5.2 V vs Li at a current density of 20 mA g^{-1}. The Braggs peaks exhibit a continuous shift that corresponds to the plains (222), (333), and (622), hence showing the occurrence of expansion and contraction of the cubic unit cell accompanying the Li-ion during the insertion and de-insertion process. The in-operando XRD data favors the occurrence of a solid-solution mechanism during charge–discharge and will remain as a single phase in the entire voltage range.[30] However, considering the other spinel materials, such as $LiNi_{0.5}Mn_{1.5}O_4$ (LNMO) and $LiMn_2O_4$, which undergo a two-phase reaction, the occurrence of a solid-solution mechanism in LCMO can be accounted for by the low cation size difference of the Mn^{3+}/Mn^{4+} (0.115 Å) and Co^{3+}/Co^{4+} (0.015 Å) which leads to the formation of a mixed phase, hence forming the solid solution. In addition, a change in lattice parameter compared to its initial value has been observed as the charge–discharge continues, owing to the structural degradation due to cation rearrangement or oxygen release.[30] Even though the solid-solution mechanism highly favors the reaction kinetics as well as rate capability, the slight structural degradation can cause a decrement in both these parameters. Adding to this, the formation of a passive CEI layer due to electrolyte decomposition can also result in sluggish Li^+ ion kinetics as well as an increase in irreversibility.

The nature of the as-formed PEDOT coating layer and its effect on the electrochemical performance of LCMO has been

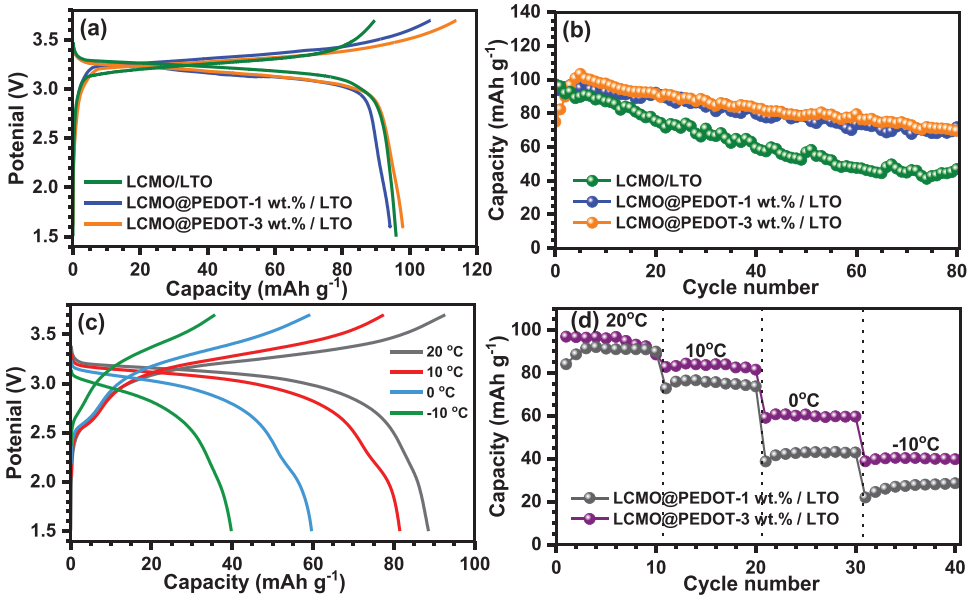

Figure 8. a) Charge–discharge curves at a current density of 20 mA g^{-1} within a potential window of 1.5–3.7 V, b) discharge capacity vs cycle number of LCMO-LTO and LCMO@PEDOT-LTO : 1–3 wt.% full-cells, c) charge–discharge curve of LCMO@PEDOT: 1–3 wt.%/LTO at different temperatures ranging from −10 to 20 °C, and d) discharge capacity vs cycle number.

revealed from the post-mortem analysis of the electrodes.[31] The powder XRD analysis (Figure S7, Supporting Information) exhibits no shift in the 2θ value, nor is there any generation of new peaks. Also, the prominent peaks corresponding to the planes (111), (311), (400), and (440) suggest the retention of the cubic crystal lattice even after the charge–discharge. The XPS analysis (Figure S8a–d, Supporting Information) of the electrodes has been carried out to analyze the surface elemental composition as well as the nature of the CEI layer formed during the charge–discharge. The deconvolution of the C 1s spectra exhibits peaks corresponding to C═C (284.4 eV), C—C (285.79 eV), and C—O (286.9 eV) for the uncycled electrodes, whereas a new peak corresponding to the C—F (292.1 eV) has been generated for the cycled electrode. The peaks assigned to the C═C and C—C at binding energies of 284.4 and 285.79 eV have been generated from the conductive polymer, PEDOT, or the conductive material (Acetylene black), whereas the peak corresponding to C—F at 292.1 eV results from the LiF that has been trapped on the surface of PEDOT. In addition, the deconvolution of O 1s spectra exhibits peaks corresponding to M(Co/Mn)—O (529.8 eV), C—O (531.9 eV), and C═O (533.8 eV). Of the various peaks, the C—O and C═O correspond to the Li_2CO_3 or C═O components of the formed CEI layer, whereas the M—O peak corresponds to the metal oxide (Mn—O, Co—O) component of the cathode material. On comparing the O 1s spectra, a slight increase in the C—O and C═O peak intensity can be observed for the cycled electrode compared to the uncycled electrode owing to the CEI formation. However, no drastic change in the M—O peak intensity can be observed by comparing the spectra of the cycled and the uncycled electrode owing to the mitigation of transition metal dissolution from the lattice. Hence, it can be further confirmed that the PEDOT coating suppresses the parasitic side reactions of the electrolyte with the cathode, thereby mitigating the issue of poor cycle stability as well as electrolyte decomposition. The FE-SEM images of the electrodes before and after cycling have been depicted in Figure S9a–f (Supporting Information). The SEM images of both electrodes exhibit a non-uniform particle size distribution. However, uniform distribution can be observed in the case of uncycled electrodes, whereas the cycled electrode depicts a non-uniformity owing to the formation of a CEI on its surface.

2.2. Full-Cell Performance

The excellent electrochemical performance of high voltage LCMO logically led to the demonstration of the possibility of using them in practical cells, *i.e.*, full-cell assembly with anode. The full cell study has been carried out using LCMO, LCMO@PEDOT- 1 wt.%, and LCMO@PEDOT- 3 wt.% against $Li_4Ti_5O_{12}$ (LTO) as the anode within a potential range of 1.5–3.7 V at a current density of 20 mA g^{-1}. Prior to the fabrication of the full-cell, the mass balance of the cathode has been adjusted with respect to the anode using the equation:

$$m_1 c_1 = m_2 c_2 \tag{4}$$

where m_1 and m_2 are the respective masses of cathode and anode active materials, c_1 and c_2 are the capacities in mAh g^{-1}. The GCD profile (**Figure 8**a,b) exhibits excellent initial discharge capacities of 96, 94, and 98 mAh g^{-1} with a capacity retention of 48, 93, and 80% after 80 cycles for LCMO/LTO, LCMO@PEDOT-1 wt.%/LTO, and LCMO@PEDOT- 3 wt.%/LTO, respectively. As expected, there is an enhancement in the electrochemical performance of LCMO@PEDOT: 1–3 wt.%/LTO compared to LCMO/LTO, since the PEDOT coating prevents the parasitic side reactions with electrolytes, thereby enhancing the cycle stability of the composite compared to pristine LCMO.

To further analyze the superior electrochemical performance of LCMO@PEDOT-1 wt.%/LTO and LCMO@PEDOT-3 wt.%/

LTO, a temperature study (Figure 8c,d) of both has been conducted within a temperature range of −10 to 20 °C. The GCD plots show that the LCMO@PEDOT-3 wt.%/LTO exhibits superior electrochemical performance compared to that of LCMO@PEDOT-1 wt.%/LTO due to the presence of a thicker polymer coating in the case of the former compared to the later. However, both the 1 and 3 wt.% exhibit poor electrochemical performance at a low temperature of −10 °C owing to the freezing-up of electrolytes, which reduces the mobility of Li^+ ions, whereas an enhancement in the electrochemical performance of both the composites can be observed at moderate temperatures of 10 and 20 °C owing to the increase in Li^+ ion mobility due to thermal agitation.

3. Conclusion

Here, we successfully demonstrated the effect of PEDOT on the electrochemical performance of LCMO. The cycling profile exhibits an enhancement in the electrochemical performance among the LCMO@PEDOT: 0.5–3 wt.% compared to pristine LCMO, among which the LCMO@PEDOT: 1–3 wt.% has been optimized owing to the excellent capacity retentions of 72 and 75% after 80 cycles. Adding to this, the Li-ion diffusion coefficient calculated from the CV and EIS shows an increase in its value as the PEDOT concentration increases from 0.5 to 3 wt.% with a magnitude in the order of $\approx 10^{-12}$ cm^2 s^{-1}. Also, the activation energy calculated from the Arrhenius plot shows an enhancement in the kinetics with an increase in the PEDOT coating, hence showing the effectiveness of the PEDOT coating. The in-situ XRD favors the occurrence of a solid-state mechanism among the LCMO@PEDOT with the occurrence of a single phase within the entire voltage range. The full-cell fabrication has been carried out with both LCMO@PEDOT and pristine LCMO against LTO as an anode. The cycling profile of LCMO@PEDOT: 1–3 wt.%/LTO exhibits excellent capacity retention of 98 and 93%, whereas the LCMO/LTO exhibits poor capacity retention of 48% after 80 cycles. In addition, the temperature study of LCMO@PEDOT/LTO: 1–3 wt.% shows an enhanced electrochemical performance at moderate temperatures of 10 and 20 °C, while the freezing-up of electrolytes results in a poor electrochemical performance at low temperatures of 0 and −10 °C. However, taking into account the future point of view, the surface coating of the high-voltage cathode has not yet been explored completely. Further, the implementation of various conductive polymers, such as PANI, PHT, etc., has to be done to improve the electrochemical performance of the cathode. In addition, combining the use of electrolyte additives such as LiDFOB,[8,12,32,33] FEC,[12,33,34], etc., along with surface modification can be considered a better strategy, as the synergetic effect of both can enhance the electrochemical performance.

4. Experimental Section

Synthesis: For the synthesis of $LiCoMnO_4$ (LCMO), a two-step procedure had been followed. In the initial step, a stochiometric amount of $Co(CH_3COO)_2.4H_2O$ (Sigma–Aldrich, ≥ 98%), $Mn(CH_3COO)_2.4H_2O$ (Sigma–Aldrich, ≥ 99%) along with 30 mL of ethanol had been dissolved in 50 mL of deionized water. To the precursor solution, a stochiometric amount of $(NH_4)_2CO_3$ (Sigma–Aldrich, 99.99%) dissolved in water was added along with magnetic stirring to form the precipitate. The solution was kept aside for the precipitate to settle down, and the precipitate was washed with distilled water and ethanol, followed by drying the sample at room temperature. The above-obtained sample was calcined in air at 400 °C for 5 h. The calcined sample was dispersed to an ethanol solution containing a stoichiometric amount of CH_3COOLi (Sigma–Aldrich, 99.95%) dissolved. A slow drying process evaporated the ethanol, and the sample was calcined in an argon atmosphere to 800 °C for 12 h.

PEDOT: PSS Coating: The PEDOT: PSS (Sigma–Aldrich) composites of LCMO had been prepared by a wet-coating strategy. The required amount of PEDOT: PSS was dissolved in deionized water, followed by the addition of LCMO. The mixture was subjected to vigorous magnetic stirring until the sample was properly dispersed in the solution. The solution was kept for a slow drying process until all the water evaporated, and further sample analysis was carried out. Based on the percentage coating of PEDOT: PSS, three different composites had been prepared and denoted as LCMO@PEDOT- 0.5 wt.%, LCMO@PEDOT- 1 wt.%, and LCMO@PEDOT- 3 wt.%.

Electrolyte Preparation: The electrolyte was prepared by mixing 2500 µL of 1M $LiPF_6$ in Ethylene carbonate (EC) and Dimethyl carbonate (1:1 weight ratio, LIPASTE, Tomiyama) along with the addition of 10 wt.% of Fluoroethylene carbonate (FEC) (Sigma–Aldrich, ≥ 99%) as the electrolyte additive in an Ar-filled Glove box with an oxygen level of >0.1 ppm. None of the salts or solvents were subjected to any sort of purification or pretreatment before usage.

Electrochemical Characterization: The full-cell and half-cell fabrication had been carried out in an Ar-filled Glovebox with both moisture and oxygen levels of >0.1 ppm. For the half-cell electrochemical study, 10 mg of LCMO was mixed, 2 mg of conductive additive (Acetylene black), and 2 mg of binder (Teflonized acetylene black-2, TAB) was properly mixed and made into a free-standing film. The film was then pressed onto a 14 mm stainless steel mesh (Goodfellow, UK), which acted as a current collector. Now, the electrode was kept in a vacuum oven at 75 °C to remove the traces of solvent. The electrode was then taken inside the glovebox and was fabricated with metallic Lithium in a CR2016 coin cell using the glass microfiber separator (Whatman, 1825-047, UK). For the fabrication of full-cell, the $Li_4Ti_5O_{12}$ (LTO) was chosen as the counter electrode.

The LTO electrode was made by mixing the active material (LTO), conductive additive (Acetylene black), and binder (PVDF) in a weight ratio of 80:10:10 in *N*-methyl-2-pyrrolidone (NMP) to form a slurry. The slurry was then coated over Aluminium foil using a doctor blade apparatus and was kept for drying overnight at 75 °C. These were then cut into 14 mm diameter electrodes and kept for vacuum drying at 75 °C, and the half-cell was fabricated against metallic Lithium. Before, the fabrication of the full cell, the LTO was subjected to 3 cycles. Then, the cell was de-crimped to remove the LTO electrode carefully. Prior to the fabrication of the full-cell, the mass of LCMO@PEDOT was calculated by mass balancing with respect to the anode. The full-cell was then fabricated and kept for electrochemical testing in a battery tester within a potential window of 1.5–3.7 V at a current density of 20 mA g^{-1}.

Material Characterization: The X-ray diffraction analysis (XRD, Rigaku, Smart lab 9 kW) was done to determine the structural characteristics of LCMO@PEDOT at a scan rate of 0.2° min^{-1} in a monochromatic Cu Kα radiation ($\lambda = 1.5406$ Å). The Raman spectral analysis (LabRam HR800 UV Raman microscope, Horiba Jobin-Yvon, France) was done to determine the material composition. The X-ray photoelectron spectroscopy (XPS, with a multilab instrument with a monochromatic Al Kα radiation hv = 1486.6 eV) was done to determine the surface composition of the sample. In addition, imaging techniques such as High-resolution transmission electron microscopy (HR-TEM, TECNAI, Philips, the Netherlands, 200 keV) and field-emission scanning electron microscopy (FE-SEM, S-4700, Hitachi, Japan) were carried out to analyze the morphology and structural features of the sample.

Supporting Information

Supporting Information is available from the Wiley Online Library or from the author.

Acknowledgements

S.S. acknowledges the Council of Scientific and Industrial Research (CSIR) for the funding. Y.-S.L. acknowledges the financial support from the National Research Foundation of Korea (NRF) grant funded by the Korean government (Ministry of Science, ICT and Future Planning) (No. RS-2023-00208361). V.A. acknowledges financial support from the Science and Engineering Research Board, a statutory body of DST, Govt. of India, through the Swarnajayanti Fellowship (SB/SJF/2020-21/12).

Conflict of Interest

The authors declare no conflict of interest.

Data Availability Statement

The data that support the findings of this study are available from the corresponding author upon reasonable request.

Keywords

cathodes, high voltages, $LiCoMnO_4$, Li-ion batteries, PEDOT

Received: June 19, 2023
Revised: September 4, 2023
Published online: September 24, 2023

[1] J. B. Goodenough, Y. Kim, *Chem. Mater.* **2010**, *22*, 587.
[2] L. X. Yuan, Z.-H. Wang, W.-X. Zhang, X.-L. Hu, J.-T. Chen, Y.-H. Huang, J. B. Goodenough, *Energy Environ. Sci.* **2011**, *4*, 269.
[3] J. B. Goodenough, *Nat. Electron.* **2018**, *1*, 204.
[4] A. Manthiram, J. B. Goodenough, *Nat. Energy* **2021**, *6*, 323.
[5] S. Sreedeep, S. Natarajan, V. Aravindan, *Curr. Opin. Electrochem.* **2022**, *31*, 100868.
[6] V. Etacheri, R. Marom, R. Elazari, G. Salitra, D. Aurbach, *Energy Environ. Sci.* **2011**, *4*, 3243.
[7] M. Zhang, N. Garcia-Araez, A. L. Hector, *J. Mater. Chem. A* **2018**, *6*, 14483.
[8] S. Sreedeep, S. Praneetha, Y. S. Lee, V. Aravindan, *ChemElectroChem* **2022**, *9*, 202200815.
[9] S. Sreedeep, S. Natarajan, Y.-S. Lee, V. Aravindan, *Electrochim. Acta* **2022**, *419*, 140367.
[10] S. Sreedeep, S. Natarajan, Y.-S. Lee, V. Aravindan, *Energy Technol.* **2022**, *11*, 1.
[11] S. Sreedeep, V. Aravindan, *Mater. Lett.* **2021**, *291*, 129609.
[12] L. Chen, X. Fan, E. Hu, X. Ji, J. Chen, S. Hou, *Chem* **2019**, *5*, 896.
[13] N. Reeves-McLaren, M. Hong, H. Alqurashi, L. Xue, J. Sharp, A. J. Rennie, R. Boston, *Energy Procedia* **2018**, *151*, 158.
[14] S. Liu, H. He, D. Zhang, C. Chang, *Int. J. Energy Res.* **2021**, *45*, 16538.
[15] K. Ariyoshi, H. Yamamoto, Y. Yamada, *Energy Fuels* **2021**, *35*, 13449.
[16] C. H. Lai, D. S. Ashby, T. C. Lin, J. Lau, A. Dawson, S. H. Tolbert, B. S. Dunn, *Chem. Mater.* **2018**, *30*, 2589.
[17] X. Ma, C. Wang, X. Han, J. Sun, *J. Alloys Compounds* **2008**, *453*, 352.
[18] Y. Chen, Y. Zhang, B. Chen, Z. Wang, C. Lu, *J. Power Sources* **2014**, *256*, 20.
[19] Q. Xue, J. Li, G. Xu, H. Zhou, X. Wang, F. Kang, *J. Mater. Chem. A* **2014**, *2*, 18613.
[20] U. D. Chavan, P. Prajith, B. Kandasubramanian, *Chem. Eng. J. Adv.* **2022**, *12*, 100416.
[21] D. Lepage, C. Michot, G. Liang, M. Gauthier, S. B. Schougaard, *Angew. Chem. – Int. Ed.* **2011**, *50*, 6884.
[22] F. Wu, J. Liu, L. Li, X. Zhang, R. Luo, Y. Ye, R. Chen, *ACS Appl. Mater. Interfaces* **2016**, *8*, 23095.
[23] Y. Li, L. Yuan, Z. Li, Y. Qi, C. Wu, J. Liu, Y. Huang, *RSC Adv.* **2015**, *5*, 44160.
[24] M. Hu, Y. Tian, J. Wei, D. Wang, Z. Zhou, *J. Power Sources* **2014**, *247*, 794.
[25] Y. Kwon, Y. Lee, S.-O. Kim, H.-S. Kim, K. J. Kim, D. Byun, W. Choi, *ACS Appl. Mater. Interfaces* **2018**, *10*, 29457.
[26] C. V. Ramana, M. Massot, C. M. Julien, *Surf. Interface Anal.* **2005**, *37*, 412.
[27] S. Brutti, J. Manzi, D. Meggiolaro, F. M. Vitucci, F. Trequattrini, A. Paolone, O. Palumbo, *J. Mater. Chem. A* **2017**, *5*, 14020.
[28] D. Zhang, J. Zhou, J. Chen, B. Xu, W. Qin, C. Chang, *Int. J. Electrochem. Sci.* **2018**, *13*, 2544.
[29] E. Markevich, R. Sharabi, H. Gottlieb, V. Borgel, *Electrochem. Commun.* **2012**, *15*, 22.
[30] C. Dräger, F. Sigel, S. Indris, D. Mikhailova, L. Pfaffmann, M. Knapp, H. Ehrenberg, *J. Power Sources* **2017**, *371*, 55.
[31] T. Kim, L. K. Ono, Y. Qi, *Adv. Mater. Interfaces* **2019**, *6*, 1801785.
[32] J. Cha, J. G. Han, J. Hwang, J. Cho, N. S. Choi, *J. Power Sources* **2017**, *357*, 97.
[33] N. Ehteshami, L. Ibing, L. Stolz, M. Winter, E. Paillard, *J. Power Sources* **2020**, *451*, 227804.
[34] R. Sharabi, E. Markevich, K. Fridman, G. Gershinsky, G. Salitra, D. Aurbach, G. Semrau, M. A. Schmidt, N. Schall, C. Bruenig, *Electrochem. Commun.* **2013**, *28*, 20.